

# Reconstruction-Determined Alkaline Water Electrolysis at Industrial Temperatures

Xiong Liu, Ruiting Guo, Kun Ni,\* Fanjie Xia, Chaojiang Niu, Bo Wen, Jiashen Meng, Peijie Wu, Jinsong Wu,\* Xiaojun Wu, and Liqiang Mai\*

Evaluating the alkaline water electrolysis (AWE) at 50–80 °C required in industry can veritably promote practical applications. Here, the thermally induced complete reconstruction (TICR) of molybdate oxygen evolution reaction (OER) pre-catalysts at 51.9 °C and its fundamental mechanism are uncovered. The dynamic reconstruction processes, the real active species, and stereoscopic structural characteristics are identified by in situ low-/high-temperature Raman, ex situ microscopy, and electron tomography. The completely reconstructed (CR) catalyst (denoted as cat.-51.9) is interconnected by thermodynamically stable (oxy)hydroxide nanoparticles, with abundant boundaries and low crystallinity. For alkaline OER, cat.-51.9 exhibits a low overpotential (282.3 mV at 20 mA cm<sup>-2</sup>, 25.0 °C) and ultrastable catalysis at 51.9 °C (250 h, with a negligible activity decay of 19.6 μV h<sup>-1</sup>). The experimental observations combined with theoretical analyses confirm the fast catalytic kinetics enabled by the co-effect of boundaries and vacancies. The coupled cat.-51.9 and MoO<sub>2</sub>-Ni hydrogen-evolving arrays provide stable electrolysis operation at 51.9 °C for 220 h. This work uncovers new reconstruction phenomenon of pre-catalysts under realistic conditions and exceptional durability of CR catalysts toward practical high-temperature AWE.

Water-electrolysis technology can realize zero CO<sub>2</sub> emission and acquire large-scale hydrogen with high purity (>99.9%), and thus potentially serves as a key component in future sustainable energy systems.<sup>[1,2]</sup> However, this technology accounts for only 4% of current hydrogen production, which is mainly attributed to its higher cost in comparison with other methods such as the conversion of natural fossil fuels.<sup>[3]</sup> For commercial water electrolysis systems, the existing key problems mainly focus on the use of efficient but exorbitant iridium, ruthenium or platinum catalysts, or economically practical nickel meshes and stainless steel with the unsatisfying activity.<sup>[4]</sup> Exploring highly active and cost-effective catalysts with good durability is imperative but challenging. Though important breakthroughs have been made recently in investigating high-efficiency first-row transition metal catalysts for oxygen and hydrogen evolution reactions (OER and HER),<sup>[5–9]</sup> a certain gap still exists between the test condition (almost at room temperature, Table S1, Supporting


Information) and the industrial one (at 50–80 °C). Therefore, it is essential to evaluate the catalytic performance and compatibility of catalysts under such harsh operating condition for further practical applications.

Rational design of HER and OER catalysts which can be well operated at industrial temperatures is highly desirable for practical alkaline water electrolysis (AWE) application. Our reported MoO<sub>2</sub>-Ni arrays exhibited a Pt-like HER activity at 25.0 °C, and the convenient synthesis route was beneficial to its mass production.<sup>[10]</sup> Such a catalyst serves as a potential candidate because its heterogeneous components may avoid agglomeration under high-temperature catalytic conditions. For anodic OER, some researchers recently evaluated the catalytic performance at 80 °C, such as NiFe-LDH<sup>[11]</sup> in alkali or CoFePbO<sub>x</sub><sup>[12]</sup> in acid, however with only ≈20 h operation. Our recent works have focused on the reconstruction chemistry of catalysts, demonstrating that the deeply/completely reconstructed (denoted as DR/CR) catalysts are a potential choice. The reported DR-NiOOH was operated well with activity decay of 0.35 mV h<sup>-1</sup> in 40 h tested at 52.8 °C.<sup>[13]</sup> In addition, the DR catalysts with abundant active species can realize high component utilization and thus high-mass-activity catalysis. Nevertheless, the lithiation

X. Liu, R. Guo, F. Xia, Dr. C. Niu, B. Wen, J. Meng, P. Wu, Prof. J. Wu, Prof. L. Mai  
State Key Laboratory of Advanced Technology  
for Materials Synthesis and Processing  
Wuhan University of Technology  
Wuhan 430070, China  
E-mail: wujs@whut.edu.cn; mlq518@whut.edu.cn

Dr. K. Ni, Prof. X. Wu  
Hefei National Laboratory for Physical Sciences at the Microscale  
School of Chemistry and Materials Sciences  
CAS Key Laboratory of Materials for Energy Conversion  
CAS Center for Excellence in Nanoscience  
iChEM (Collaborative Innovation Center of Chemistry  
for Energy Materials)  
University of Science and Technology of China  
Hefei, Anhui 230026, China  
E-mail: nikun@ustc.edu.cn

Prof. L. Mai  
Foshan Xianhu Laboratory of the Advanced Energy Science  
and Technology Guangdong Laboratory  
Xianhu hydrogen Valley  
Foshan 528200, China

 The ORCID identification number(s) for the author(s) of this article can be found under <https://doi.org/10.1002/adma.202001136>.

DOI: 10.1002/adma.202001136

synthesis route is not suitable for amplifying production, and its stable operation time is still far from the practical application with a prolonged duration (>1000 h). Surface reconstruction commonly exists in the transition-metal-based catalysts<sup>[14–16]</sup> (called as pre-catalysts<sup>[17]</sup>) with a limited reconstruction degree (<10 nm) when tested at room temperature. This is attributed to the reconstruction termination caused by the dense reconstruction layer and thus limited mass transport.<sup>[18,19]</sup> However, the reconstruction of pre-catalysts would probably be promoted and deepened at 50–80 °C. Therefore, the real catalytic species and reconstruction mechanisms between conventional and industrial tests may be different. This inspires us to acquire CR catalysts under high-temperature electro-oxidation condition. However, evaluating catalysts under industrial conditions is still in its infancy.

Herein, the reconstruction chemistry of pre-catalysts during OER at industrial temperatures is uncovered, and the thermally induced complete reconstruction (TICR) mechanism is identified. Taking nickel molybdate pre-catalyst as an example, the reconstruction-driven CR catalysts display high-activity and ultrastable properties during alkaline OER at 25.0 and 51.9 °C. Thermally induced loose structure of reconstruction layer is the key to realizing deep penetration of solution and subsequent catalytic oxidation reactions. The reconstructed multilevel architecture (marked as cat.-51.9 thereafter) is interconnected by ≈5 nm (oxy)hydroxide nanoparticles (NPs). Abundant grain boundaries and vacancies exist in these NPs, and further theoretical analyses confirm the boundary–vacancy co-effect on lowering the OER barriers. The MoO<sub>2</sub>-Ni cathode exhibits high-efficiency and durable HER catalysis at 25.0 and 51.9 °C, and the coupled self-supported array AWE system can operate steadily at 51.9 °C. The boundaries within anodic cat.-51.9 (i.e., grain boundary) and cathodic MoO<sub>2</sub>-Ni (i.e., phase boundary) serve as active catalytic sites and help to avoid aggregation which leads to high catalytic stability. Accordingly, we highlight the potential application of such an array system in high-temperature AWE.

Evaluating OER pre-catalysts at industrial temperatures is crucial because of its possible different reconstruction result compared with that tested at room temperature. Here, NiMoO<sub>4</sub> was rationally selected as the pre-catalyst, due to its proven post-OER structure with ≈5 nm-thick dense shell of (oxy)hydroxide as real catalytic species.<sup>[13]</sup> First, the well-ordered NiMoO<sub>4</sub> nanowire arrays anchored on the skeleton of nickel foam (NiMoO<sub>4</sub>/NF) were prepared via a hydrothermal-calcination method, which refers to our previous work.<sup>[10]</sup> The NiMoO<sub>4</sub> nanowires are ≈150 nm in diameter with high crystallinity confirmed by the selected area electron diffraction (SAED) pattern (Figure S1, Supporting Information). The synthesis is scalable with >250 cm<sup>2</sup> in total in one pot for potential mass production (Figure S2, Supporting Information). To reveal the effects of temperature-dependent reconstruction of pre-catalysts during alkaline OER, the chronopotentiometric measurements were conducted via a temperature-controlled three-electrode device (Figure S3a, Supporting Information) to capture the real-time potential change. The detected solution temperatures are shown in Figure S3b (Supporting Information). These measurements were initially operated at 25.0 °C for 12 h, and then tested at

T °C for 36 h, and finally tested at 25.0 °C for 12 h (Figure 1a). Here, T °C (T = 25.0, 32.4, 39.6, 51.9) represents the actual temperatures of alkaline solution measured by a digital display thermometer. For NiMoO<sub>4</sub>/NF pre-catalyst and nickel foam, the final products after such tests are denoted as cat.-T and NF-T, respectively. At 25.0 °C and to achieve a current density of 10 mA cm<sup>-2</sup>, the overpotential ( $\eta_{10}$ ) of cat.-25.0 is as high as 436.3 mV after continuous 60 h chronopotentiometric testing. This result is attributed to the less reconstructed OER species on the NiMoO<sub>4</sub> surface, and the dense reconstruction layer generally renders the inner part ineffective. Replacing with a fresh NiMoO<sub>4</sub>/NF, the  $\eta_{10}$  is repeatable as 449.7 mV at 25.0 °C. When rising to 32.4 °C, the measured potential values gradually decrease. Besides, the potentials still decrease when the solution maintains at 32.4 °C, indicating the thermally induced formation of OER-active species. As expected, with more active species, the catalyst displays a 60.5 mV decrease after testing at 32.4 °C and recovering to 25.0 °C. Similarly, the potential difference ( $\Delta V$ ) values after 39.6 and 51.9 °C treatments increase, demonstrating the enhanced OER activity. Especially, when treated at 51.9 °C and in the 48-hour stage, the potentials are unchanged at 0.547 V versus Hg/HgO electrode ( $V_{\text{Hg}/\text{HgO}}$ ), indicating the termination of reconstruction. Such a reconstruction is complete which is proved hereinafter. The similar processes continue during thermal treatments, which are schematically illustrated in Figure 1b. Summarily, the temperature-dependent reduced potentials of  $\Delta V$  are calculated based on the potential difference at 60 and 12 h (Figure S3c, Supporting Information). After treatments at 25.0, 32.4, 39.6, and 51.9 °C, the  $\Delta V$  are -0.5, 60.5, 94.2, and 117.2 mV, respectively. Notably, the NF-51.9 shows an increased potential after treatment at 51.9 °C. Meanwhile, the blank nickel foam shows the negligible OER activity tested at 25.0 °C (Figure S3d, Supporting Information). This suggests that the decreased potentials for cat.-T samples are attributed to the thermally driven formation of more OER-active species derived from NiMoO<sub>4</sub>. In addition, the carbon cloth substrate is not recommended for use during such high-temperature oxidation conditions, because it would collapse due to the electro-oxidation induced stripping (Figure S3e, Supporting Information).

As discussed above, a TICR strategy is applied to promote the full activation of pre-catalysts, and thus achieving significantly improved catalysis performance. After above 60 h chronopotentiometric testing, the linear sweep voltammetry (LSV) measurements were further operated using a fresh Hg/HgO electrode to evaluate OER activity of these activated catalysts (Figure 1c). After higher temperature treatments, lower overpotentials are required to achieve the same current density (Figure 1d). Among all the catalysts, the cat.-51.9 exhibits the lowest overpotentials ( $\eta_{15} = 274.1$  mV,  $\eta_{20} = 282.3$  mV,  $\eta_{25} = 288.0$  mV,  $\eta_{30} = 293.2$  mV) with the corresponding Tafel slope of 47.8 mV (Figure 1e). The overpotential values at 10 mA cm<sup>-2</sup> for typical commercial IrO<sub>2</sub>/C catalyst were generally in the range of 310–350 mV as reported.<sup>[18,20]</sup> Therefore, the cat.-51.9 can serve as a potential IrO<sub>2</sub>-substituted candidate. The influence of the mass loadings of the supported NiMoO<sub>4</sub> can be negligible because a set

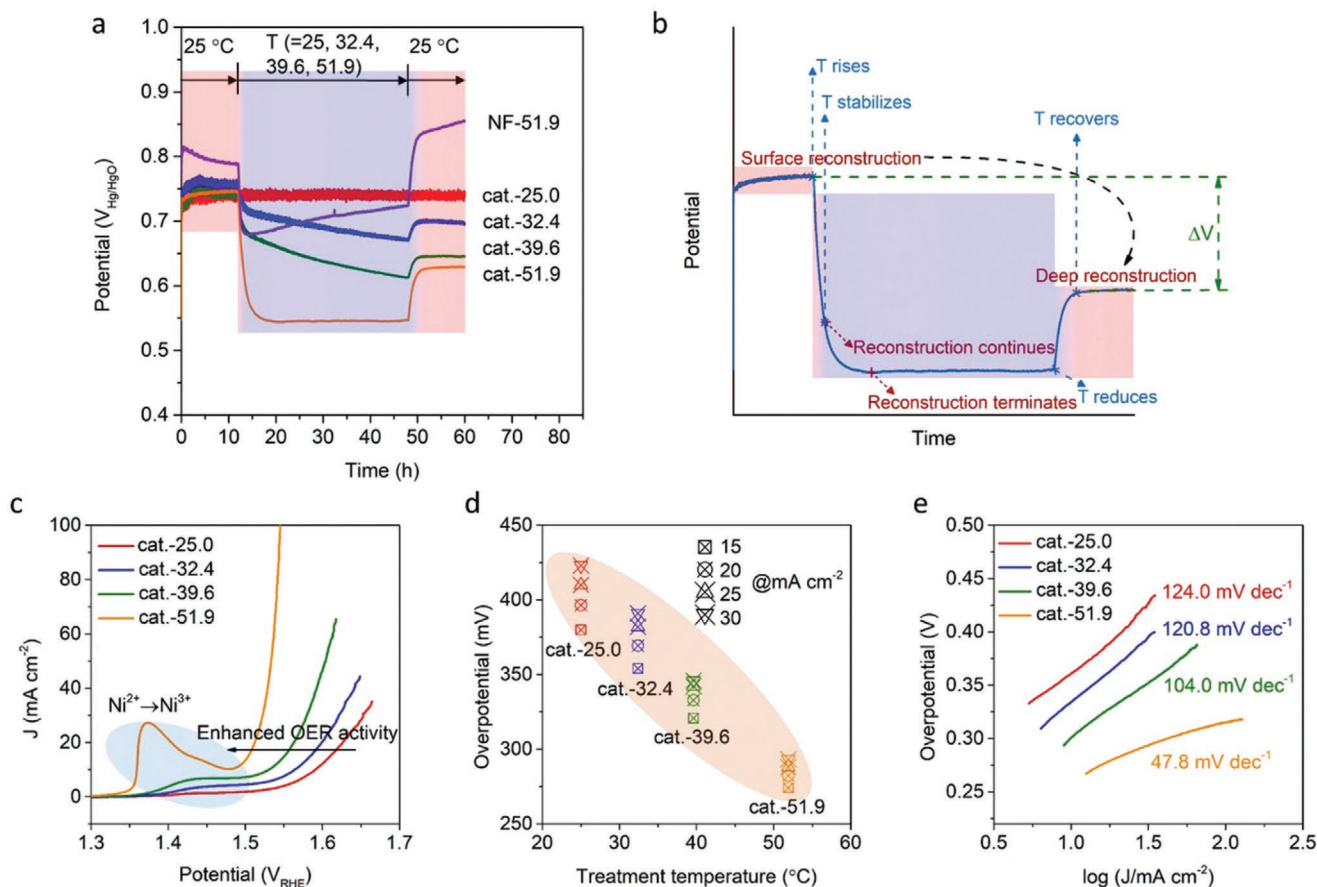


**Figure 1.** a) Chronopotentiometric measurements of NiMoO<sub>4</sub> pre-catalyst and nickel foam (NF) at 10 mA cm<sup>-2</sup> in 1 M KOH with solution temperatures of  $T$ . In detail, the initial 0–12 h stage was tested at 25.0 °C, and the next 12–48 h stage was tested at  $T$  °C ( $T = 25.0, 32.4, 39.6, 51.9$ ), and the final 48–60 h stage was tested at 25.0 °C. The finally obtained catalysts are denoted as cat.- $T$  for subsequent performance evaluation. For NF- $T$  sample,  $T$  is 51.9. b) Schematic diagram for the temperature-dependent potential curve, which associates with the thermally induced reconstruction results. The reduced potential  $\Delta V$  is based on the difference value of potentials at 60 and 12 h in (a). c–e) LSV curves, the corresponding overpotentials, and Tafel values of cat.- $T$  tested at 25.0 °C, respectively.

of measurements is based on one foam sample. Therefore, the reduced overpotentials and faster OER kinetics of cat.- $T$  ( $T > 25.0$  °C) are attributed to the thermally driven activation of dead pre-catalysts. Especially, the obtained cat.-51.9, which is confirmed to be NiOOH hereinafter, is even comparable or superior to those carefully designed catalysts, such as element doping and heterostructure construction (Table S1, Supporting Information).

To uncover the effect of temperature on the reconstruction degree, the post-OER cat.- $T$  samples were characterized by a series of technologies. As shown in the high-resolution transmission electron microscopy (HRTEM) image (Figure 2a), the clear reconstruction layer of  $\approx 6$  nm is observed in cat.-25.0, which is consistent with the previous result.<sup>[13]</sup> As revealed, the reconstructed region belongs to NiOOH species. The reconstruction degree is deepened for cat.-32.4 ( $\approx 19$  nm), which is further deepened for cat.-39.6 and complete for cat.-51.9 (Figure 2b–d). In detail, the indexed (202) plane in the core region of nanowire refers to the NiMoO<sub>4</sub> phase (JCPDS No. 86-0361), and the (310) and (111) planes in the shell region refer to the NiOOH phase. The white dotted lines represent the observed NiMoO<sub>4</sub>-NiOOH boundary. For cat.-51.9, no obvious boundary is found, and the

obtained NiOOH nanowires show  $\approx 5$  nm NPs-interconnected structure with abundant grain boundaries. Such a completely reconstructed structure in cat.-51.9 is identified as NiOOH phase, and all the observed lattice fringe spacings are well-indexed to the lattice planes of orthorhombic NiOOH (JCPDS No. 27-956) from HRTEM image (Figure 2d). To take a panoramic view of the composition changes for the whole nanowire, the elemental mappings of single cat.- $T$  nanowire were collected by scanning transmission electron microscopy-energy-dispersive X-ray spectroscopy (STEM-EDX) (Figure 2e–h). The Mo-element distribution in the radial region becomes increasingly narrow with the rising of treatment temperatures, and ultimately disappears for cat.-51.9. The Mo signals are undetected in the cat.-51.9 via EDX spectrum, suggesting the full leaching of Mo species and complete reconstruction of NiMoO<sub>4</sub> pre-catalyst (Figure S4a,b, Supporting Information). As directly confirmed by the high-angle annular dark-field STEM (HAADF-STEM) image (Figure S4c, Supporting Information), the cat.-51.9 is featured by  $\approx 5$  nm NPs-interconnected nanowire structure. The temperature-dependent reconstruction results were further studied by TEM images and SAED patterns (Figure S5, Supporting Information), showing the large NiMoO<sub>4</sub> crystals gradually transform into (oxy)hydroxide



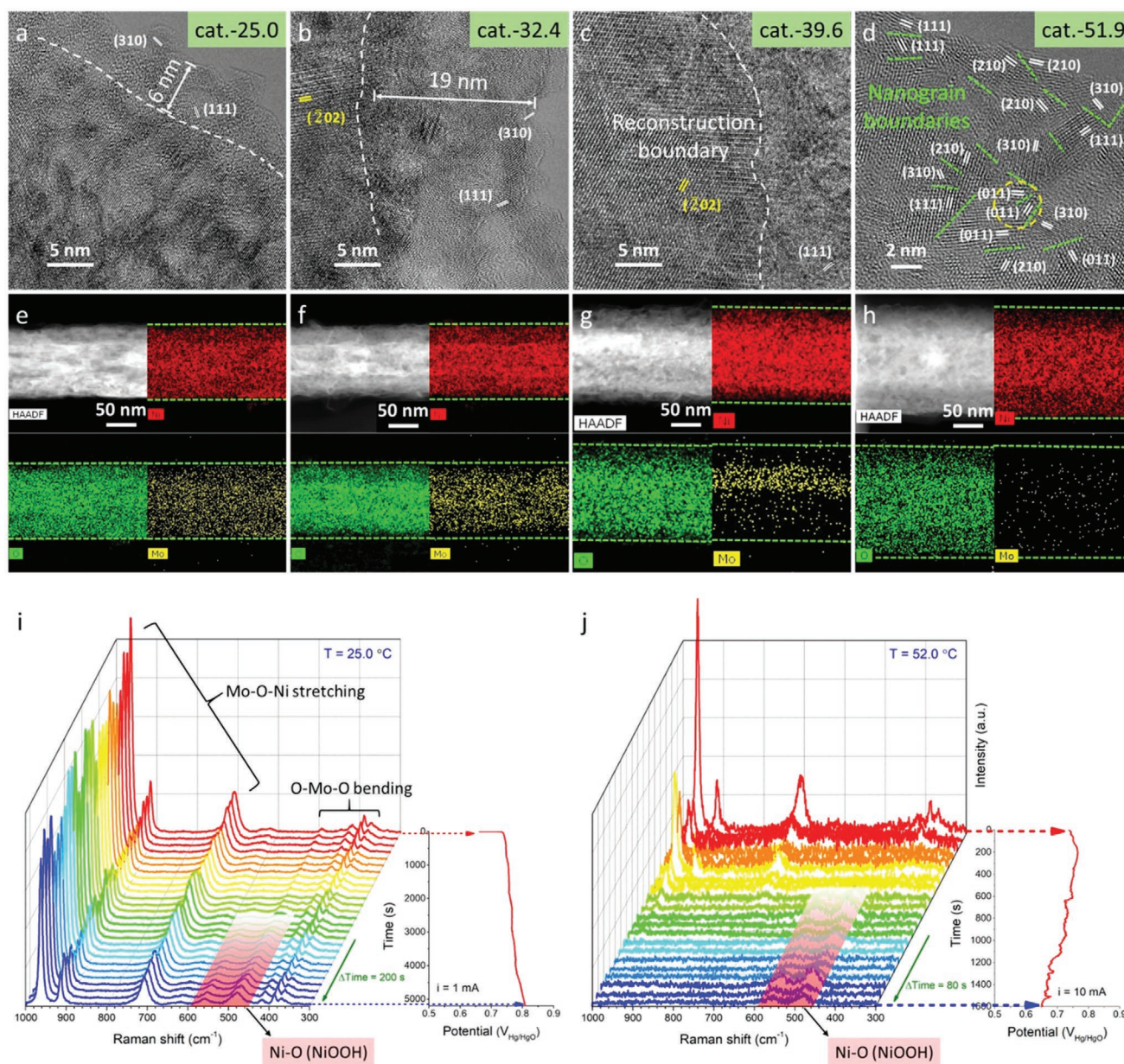


**Figure 2.** a–d) HRTEM and e–h) HAADF-STEM images and the corresponding elemental mappings of cat.- $T$  ( $T = 25.0, 32.4, 39.6, 51.9$ ). The white dotted lines in (a–c) represent the obviously observed reconstruction boundary. i) In situ low-temperature Raman spectra and the corresponding chronopotentiometric curve of  $\text{NiMoO}_4$  pre-catalyst with the interval time of 200 s in 1 M KOH at 25.0 °C. j) In situ high-temperature Raman spectra and the corresponding chronopotentiometric curve of  $\text{NiMoO}_4$  pre-catalyst with the interval time of 80 s in 1 M KOH at 52.0 °C.

NPs with the increased treatment temperatures. In the end, such a strategy effectively achieves complete reconstruction of  $\text{NiMoO}_4$  pre-catalyst, and ultimately the morphology-conformal  $\text{NiOOH}$  serves as a stable catalyst.

To further uncover the real active species of  $\text{NiMoO}_4$  pre-catalyst during OER catalysis, in situ Raman measurements were conducted. The silicone rubber heating plate below the poly(tetrafluoroethylene) (PTFE) slab was used to control the solution temperature, which was accurately measured by a digital display thermometer (Figure S6a, Supporting Information). Before Raman measurements, the temperatures between heating equipment and solution were associated (Figure S6b,

Supporting Information). Next, the chronopotentiometric measurements were conducted and the Raman signals were collected simultaneously. When carried out at 25.0 °C and applied oxidizing current, two new weak peaks centered at 474 and 554  $\text{cm}^{-1}$  belonging to  $\text{NiOOH}$  gradually appear (Figure 2i). Nevertheless, the strong peaks at 385, 705, 910, and 960  $\text{cm}^{-1}$  belonging to  $\text{NiMoO}_4$  are still predominant. Contrarily, when carried out at 52.0 °C, the peaks for  $\text{NiMoO}_4$  completely disappear within 10 min (Figure 2j). Then only the peaks of  $\text{NiOOH}$  emerge and remain, suggesting the complete reconstruction of  $\text{NiMoO}_4$ . These results are in good agreement with the above electron microscopy observations. In addition, different from



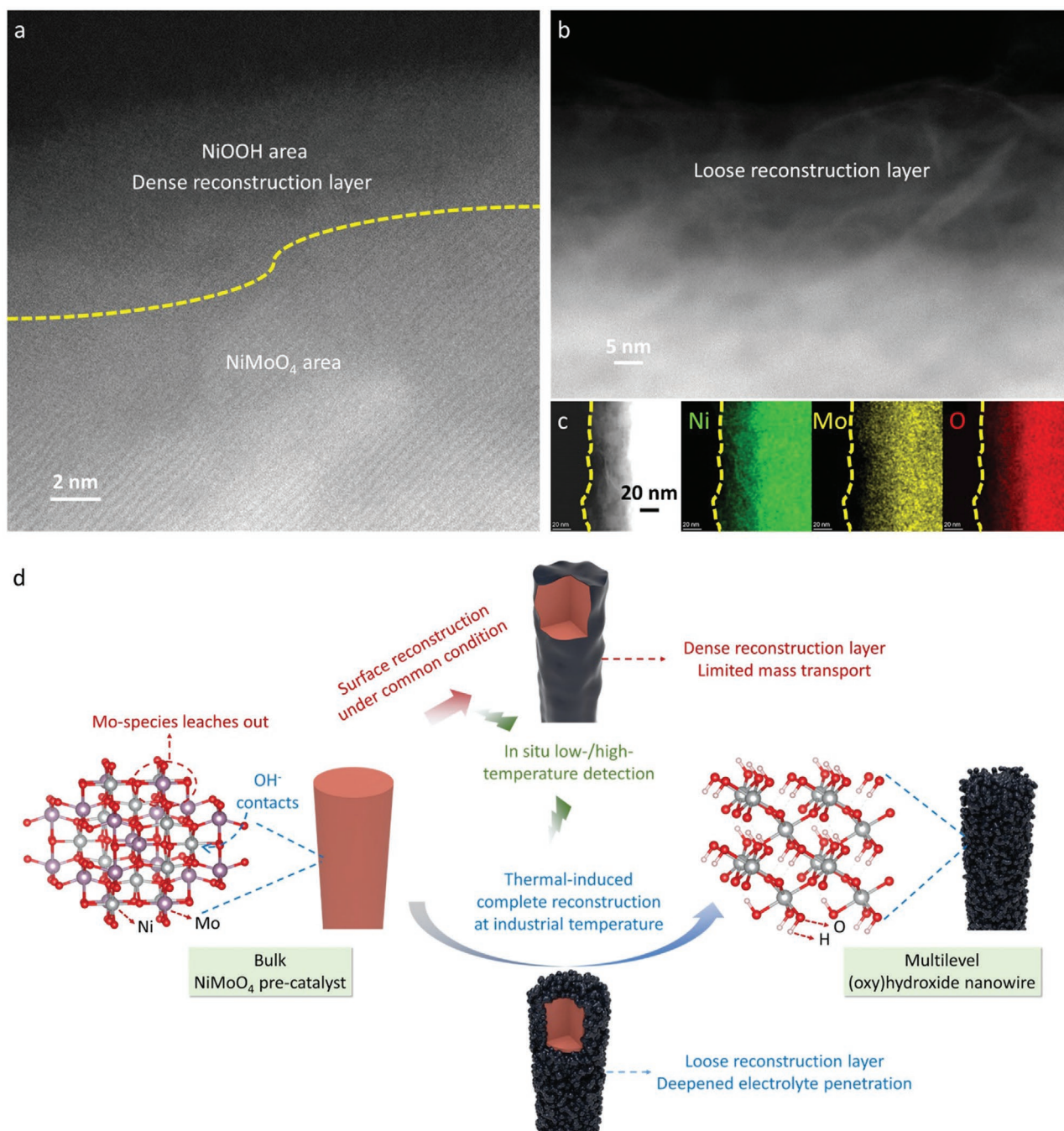


**Figure 3.** a) HAADF-STEM image of NiMoO<sub>4</sub> pre-catalyst after chronopotentiometric measurement at 10 mA cm<sup>-2</sup> at 25.0 °C for 12 h. b) HAADF-STEM image of NiMoO<sub>4</sub> pre-catalyst after chronopotentiometric measurement at 10 mA cm<sup>-2</sup> at 25.0 °C for 12 h and then rising to 51.9 °C. c) HAADF-STEM image and the corresponding elemental mappings of sample in (b), showing the dissolution of Mo species on the surface. d) Schematic diagram for the two reconstruction results of NiMoO<sub>4</sub> pre-catalyst under low-/high-temperature electro-oxidation conditions.

the one tested at 25.0 °C, the recorded chronopotentiometric data at 52.0 °C show the gradually decreased potential. This is attributed to the production of more and more OER-active (oxy) hydroxide species.

To recognize the origin of thermally driven complete reconstruction, ex situ HAADF-STEM characterizations were carried out to investigate the variation of near-surface region during different stages of chronopotentiometric testing. The dense

reconstruction layer is formed on the NiMoO<sub>4</sub> surface after testing at 25.0 °C (Figure 3a), which blocks the deep penetration of solution and causes the limited mass transport, and thus results in its terminated reconstruction. Such a phenomenon also exists in other reported pre-catalysts, such as phosphide<sup>[18]</sup> and hydroxide<sup>[21]</sup>. When rising the electro-oxidation temperature to 51.9 °C, the surface is converted into highly porous and loose structure (Figure 3b). Almost no Mo element exists

on the edge of nanowire (Figure 3c), and the observed loose layer could thus be attributed to the leaching of Mo species. As schematically illustrated in Figure 3d, two reconstruction results are displayed under low-/high-temperature conditions. When NiMoO<sub>4</sub> is reconstructed to NiOOH, the reconstruction processes include: 1) the dissolution of Mo species due to alkali etching; 2) the reaction between Ni and the hydroxyl group from solution to form hydroxide; 3) the formation of (oxy)hydroxide via the subsequent electro-oxidation reaction. The high diffusion barrier of Mo species in crystalline materials<sup>[16]</sup> leads to the slow reconstruction rate and a dense layer by reconstruction. Therefore, the thermal system can accelerate the leaching of Mo species, and thus leading to the formation of loose reconstruction layer. Such a loose structure is solution accessible with effective mass transport, triggering a chain of reconstructions till complete reconstruction and resulting in the NPs-interconnected structure.

Chen group discovered that the Fe/P incorporation can induce the lattice distortion and thus affected the formed (oxy) hydroxide species after reconstruction.<sup>[22,23]</sup> The roles of Mo in NiMoO<sub>4</sub> pre-catalyst are similar. Actually, the highly disordered structure is observed in the right region near the reconstruction boundary for cat.-39.6 (Figure 2c). The outermost layer of cat.-39.6 nanowire displays the low-crystalline nanograin structure (Figure S7, Supporting Information). These results suggest the highly disordered region serves as the intermediate with Mo incorporation, and then transforms into low-crystalline species after further oxidation. It should be noted that the Mo species is undetected in cat.-51.9, suggesting the complete leaching of Mo species during reconstruction. In addition, the self-reconstructed counterpart was demonstrated to have rich vacancies.<sup>[16]</sup> Therefore, our completely reconstructed catalyst possesses the unique properties of simplex component, open 3D framework, ultrasmall NPs-interconnected structure with abundant vacancies and boundaries. Besides NiMoO<sub>4</sub>, the complete reconstruction of CoMoO<sub>4</sub> pre-catalyst was also achieved via such a TCR strategy (Figure S8, Supporting Information). The obtained CR CoOOH serves as the final and stable catalyst, and shows higher OER activity than that of the incompletely reconstructed CoMoO<sub>4</sub>@CoOOH.

Compared to that in ex situ reconstruction, the in situ reconstruction leads to the formation of a more effective structure with high density of boundaries and vacancies. Such an interesting phenomenon is uncovered with two sets of catalytic results (Figure 4a), which were closely related to the order of reconstruction. When the oxidizing potential was applied at 51.9 °C and then tested at 25.0 °C, a lower potential was obtained. This process is herein called in situ reconstruction, during which the deep etching and electro-oxidation processes simultaneously exist. It results in ≈5 nm NPs with abundant boundaries and low crystallinity (Figure 4b,c; Figure S9a, Supporting Information). Meanwhile, ex situ reconstruction refers to the process that the oxidizing potential was applied after the completion of etching reaction at 51.9 °C. It results in the formation of larger particles with fewer grain boundaries and high crystallinity (Figure 4d,e; Figure S9b, Supporting Information). Actually, the etching reaction between NiMoO<sub>4</sub> and KOH solution results in the formation of Ni(OH)<sub>2</sub> (Figure S10, Supporting Information), which evolves into (oxy)hydroxide

species after electro-oxidation. Such a reaction results in the large sheet-interconnected nanowire structure (Figure S11, Supporting Information), and thus the ex situ catalyst displays fewer grain boundaries and higher crystallinity after reconstruction. X-ray photoelectron spectroscopy (XPS) measurements of two samples were carried out to characterize the surface oxygen vacancies (Figure 4f). Three typical XPS peaks at 529.3, 530.9, and 532.7 eV via O 1s deconvolution are observed, corresponding to the metal-oxygen bonds, defects, and surface-adsorbed oxygen species, respectively.<sup>[24,25]</sup> Similar proportion of defect-relative peak suggests the existence of abundant oxygen defects in both samples. The catalyst produced by in situ reconstruction requires a lower overpotential when compared to that by ex situ reconstruction (Figure S12a, Supporting Information). Such a difference in their activity supports the positive effects of grain boundaries on OER, which can affect the real activity of catalyst under working condition. The effects of grain boundaries will be discussed later. Besides, the charge transfer resistance ( $R_{ct}$ ) values are calculated to be 1.73 and 5.3 Ω for in situ and ex situ catalysts, respectively (Figure S12b, Supporting Information). Such a smaller  $R_{ct}$  value for in situ formed catalyst suggests its charge transportation is much faster at the catalyst-electrolyte interface during OER.

OER overpotential of NiOOH species was previously predicted by density function theory (DFT) calculations, showing unexpectedly similar values on different surfaces, e.g. 1.04 V on the (101) surface<sup>[13]</sup> and 0.96 V on the (01 $\bar{1}$ 2) surface<sup>[26]</sup>. However, the gap between theoretical prediction and experimental overpotential (≈0.27 V) observed in this work is large, indicating that the traditional ideal surface model cannot describe the chemical environment of active site sufficiently. To provide further insights into the better catalytic performance for the in situ reconstruction catalyst, the effects of grain boundaries and vacancies which include O vacancy ( $V_O$ ) and OH vacancy ( $V_{OH}$ ) on the OER kinetics were considered. Six different configurations, including NiOOH (011), NiOOH (011) with  $V_O$ , NiOOH (011) with  $V_{OH}$ , NiOOH (011)-NiOOH (011) twin boundary, boundary with  $V_O$ , and boundary with  $V_{OH}$ , were judiciously constructed. The establishment of the NiOOH (011)-NiOOH (011) twin boundary model (Figure S13, Supporting Information) was based on the experimental observation from HRTEM image labelled by yellow dotted circle in Figure 2d. As shown in Figure 4g–j, the O vacancy around boundary serves as the active site. The rate determining step (RDS) changes from the formation of O\* step (step 2), as commonly considered in NiOOH species, into the formation of OOH\* step (step 3) with largest Gibbs free energy difference ( $\Delta G_{max}$ ) of 1.772 eV due to the enhanced oxygen adsorption. In comparison, the  $\Delta G_{max}$  for NiOOH (011) is as large as 2.119 eV, and the value is still not optimistic even after singly introducing O/OH vacancy or boundary as summarized (Figure 4k) with the corresponding optimized OER pathways (Figure S14, Supporting Information). This suggests that the boundary–vacancy co-effect can promote the high OER activity. Our predicted overpotential of 0.542 V on boundary–vacancy co-existence model is much closer to the experimental value when compared to the previous reports on ideal surfaces. The projected density of states (PDOS) calculations accompanied with crystal orbital Hamilton population (COHP) analysis were further conducted (Figure 4l; Table S2



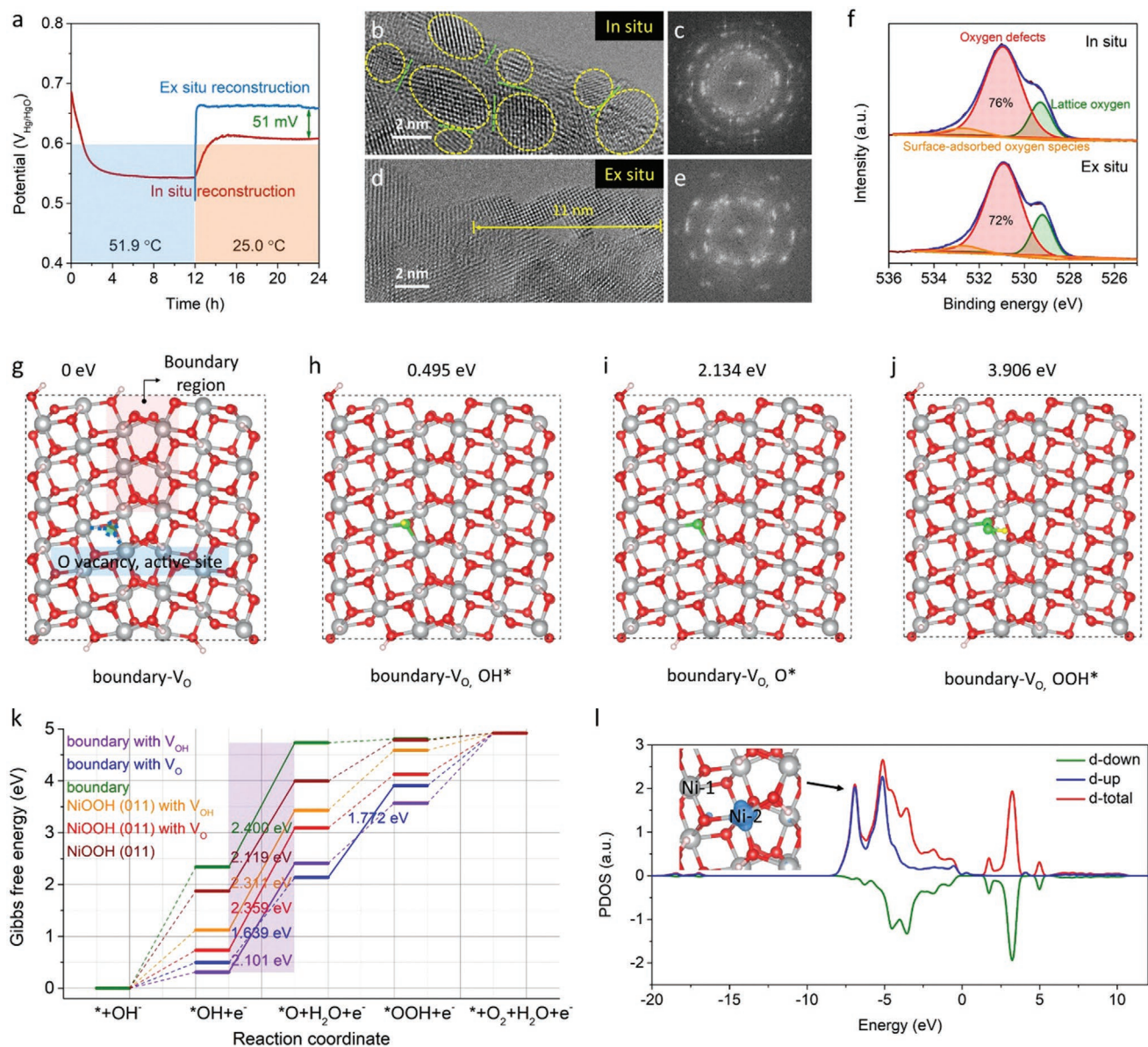


**Figure 4.** a) Chronopotentiometric measurements at 10 mA cm<sup>-2</sup> in 1 M KOH. For in situ reconstruction, the NiMoO<sub>4</sub> pre-catalyst was first measured at 51.9 °C and then at 25.0 °C, and the obtained catalyst is called an in situ catalyst. For ex situ reconstruction, the NiMoO<sub>4</sub> was first soaked in 1 M KOH at 51.9 °C and then measured at 25.0 °C, and the obtained catalyst is called an ex situ catalyst. b–e) HRTEM images and the corresponding fast Fourier transform patterns of in situ catalyst (b,c) and ex situ catalyst (d,e). f) O 1s XPS spectra of in/ex situ catalysts. g) Model of NiOOH (011)–NiOOH (011) twin boundary structure with O vacancy, showing the O vacancy site in the boundary region. h–j) DFT-calculated models with the optimal structures for intermediate products. k) Free energy of each reaction step on six different models, considering the effects of boundary, O/OH vacancies on OER. l) PDOS calculation of d band of Ni-2 atom near the O vacancy site in the boundary region in boundary with V<sub>O</sub> model. Inset: the partial charge density drawn from –7 to –6.8 eV with iso-surface value of 0.025 e<sup>-</sup> bohr<sup>-3</sup>, corresponding to the PDOS peak at –6.9 eV.

and Figure S15, Supporting Information). For boundary with V<sub>O</sub> model, the additional d electron states of Ni-2 atom at –6.9 eV energy level contributes to the enhancement of Ni–O\* bond. In addition, the band decomposed charge density (inset in Figure 4l) clearly shows that the electron states around –6.9 eV, e.g. from –7 to –6.8 eV, are mainly attributed to the localized defect state of Ni atom at oxygen vacancy and boundary.

Surface and interface control in nanoparticle provide the optimized catalysis.<sup>[27]</sup> There is co-existence of abundant boundaries

and vacancies for the in situ reconstruction catalyst. Vacancy engineering is common for high-efficiency catalysts, while the investigation of boundary is relatively less. In addition, the reported grain boundaries of catalysts are generally at the sub-/micrometer scale of >100 nm and functions in CO<sub>2</sub> reduction<sup>[28]</sup> and HER catalysis.<sup>[29]</sup> Grain boundary at the nanoscale (<100 nm) can greatly increase the total number of boundary accompanied with abundant vacancies, which promotes high catalytic performance reflected in the highly fragmented copper

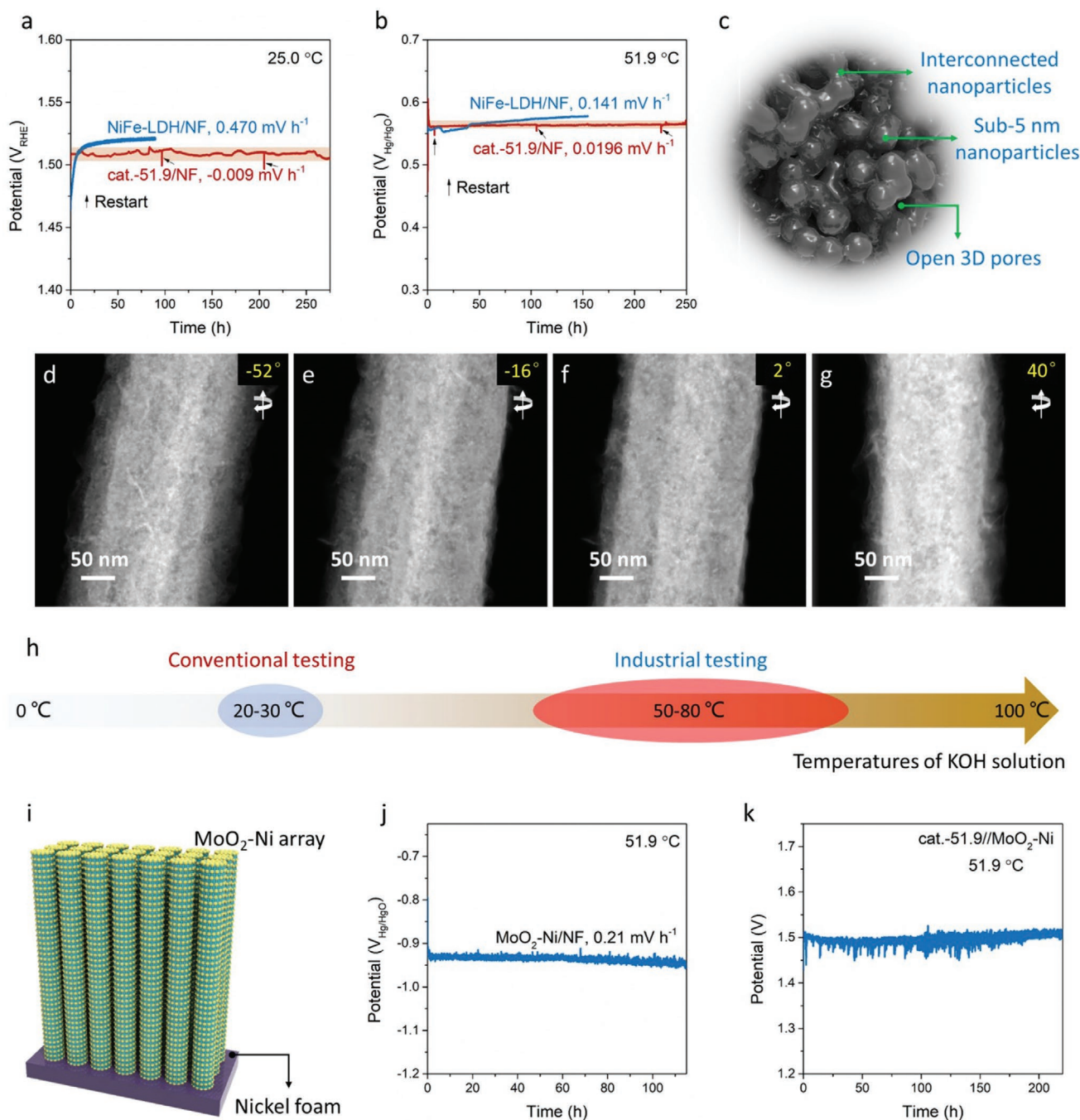


**Figure 5.** a,b) Chronopotentiometric measurement of cat.-51.9 and NiFe-LDH catalysts tested at  $10 \text{ mA cm}^{-2}$  in  $1 \text{ M KOH}$  at  $25.0 \text{ }^\circ\text{C}$  (a) and  $51.9 \text{ }^\circ\text{C}$  (b). c) Schematic diagram of NPs-interconnected structure with open 3D pores. d–g) Representative HAADF-STEM images via electron tomography of single cat.-51.9 nanowire after long-term stability measurement in (b). h) The conventional condition (almost at room temperature) has a certain gap with the industrial one (at  $50\text{--}80 \text{ }^\circ\text{C}$ ). i) Schematic diagram of  $\text{MoO}_2\text{-Ni}$  arrays on the nickel foam. j) Chronopotentiometric measurement of  $\text{MoO}_2\text{-Ni}$  heterostructured nanowire arrays at  $10 \text{ mA cm}^{-2}$  in  $1 \text{ M KOH}$  at  $51.9 \text{ }^\circ\text{C}$ . k) Durability evaluation of high-temperature water electrolysis based on the cat.-51.9 (anode) and  $\text{MoO}_2\text{-Ni}$  (cathode) array system at  $10 \text{ mA cm}^{-2}$  in  $1 \text{ M KOH}$  at  $51.9 \text{ }^\circ\text{C}$ .

structures<sup>[30]</sup> and our obtained cat.-51.9. Therefore, this work also highlights the important engineering of vacancy and nanoscale grain boundary toward high-efficiency catalysis.

To probe the stability of cat.-51.9, the chronopotentiometric measurements were sequentially performed. Herein, the cat.-51.9 catalyst for long-term stability test was obtained by

direct electro-oxidation of  $\text{NiMoO}_4/\text{NF}$  at  $51.9 \text{ }^\circ\text{C}$  for 24 h via chronopotentiometric measurement at  $10 \text{ mA cm}^{-2}$ . Actually, the test in Figure 1a has already reflected the excellent stability of cat.-51.9 during the final-stage test at  $25.0 \text{ }^\circ\text{C}$ . As presented in Figure 5a, the OER potentials at  $25.0 \text{ }^\circ\text{C}$  are stable in  $1.50\text{--}1.51 \text{ V}$  versus reversible hydrogen electrode ( $V_{\text{RHE}}$ )



for over 275 h (>11 days), indicating the ultrastable catalysis of cat.-51.9. Such a durability time is much longer than that of recently reported catalysts, which is generally below 100 h (Table S1, Supporting Information). The deposited NiFe-LDH nanosheet array on the nickel foam (NiFe-LDH/NF), one of the best catalysts reported so far,<sup>[31–33]</sup> was also tested for comparison. Though the NiFe-LDH/NF displays the superior OER activity than that of the cat.-51.9 in the initial stage, its activity decay ( $0.470 \text{ mV h}^{-1}$ ) is higher than the latter ( $-0.009 \text{ mV h}^{-1}$ ). To satisfy the potential commercial AWE applications, the high thermal stability at 50–80 °C is required.<sup>[2,8]</sup> Due to the limited affordable temperature range of Hg/HgO electrode, the KOH solution with 51.9 °C was applied here. As a result, the cat.-51.9 delivers the potentials of  $\approx 0.56 V_{\text{Hg/HgO}}$ , and can retain this catalytic activity for 250 h (Figure 5b). Similarly, the cat.-51.9 exhibits a slower activity decay ( $0.0196 \text{ mV h}^{-1}$ ) than that of NiFe-LDH/NF ( $0.141 \text{ mV h}^{-1}$ ). The cat.-51.9 displays excellent corrosion resistance and high-temperature component/catalytic stability for alkaline OER. These are attributed to the high-temperature stable (oxy)hydroxide phase uncovered by in situ high-temperature Raman and open 3D porous interconnected structure which could promote the gas diffusion (Figure 5c). Its well-remained NPs-interconnected structure was further revealed by electron tomography (Figure 5d–g, also see Video S1 in the Supporting Information) and other characterizations in Figure S16 (Supporting Information).

Evaluating the AWE performance at industrial temperatures (50–80 °C) can veritably promote its potential industrial applications (Figure 5h), thus it is also necessary to explore a kind of high-efficient HER catalyst that can stably catalyze under such harsh condition. Our reported MoO<sub>2</sub>-Ni heterostructured nanowire arrays grown on the nickel foam (MoO<sub>2</sub>-Ni/NF) were selected and schematically illustrated in Figure 5i. It was confirmed with a Pt-like HER activity at 25.0 °C,<sup>[10]</sup> and its stability was also first evaluated at 50–80 °C in this work. As shown in Figure 5j, such a catalyst can catalyze at least 115 h at 51.9 °C. While pairing it with the cat.-51.9, the coupled water electrolysis array system can maintain the cell voltage of  $\approx 1.49 \text{ V}$  for 220 h (Figure 5k), and the corresponding LSV curve is shown in Figure S17 (Supporting Information). This applicable testing emphasizes the importance of evaluating catalytic performance at industrial temperatures, suggesting the potential applications of array electrodes in commercial water electrolysis system.

In summary, we uncovered the different reconstruction phenomena of pre-catalysts during OER at room temperature and industrial temperature. The (oxy)hydroxide catalysts derived from molybdate pre-catalysts were fabricated via the thermally induced complete reconstruction. The evolution of morphology, microstructure, and phase structure has been studied by in situ low-/high-temperature Raman and electron tomography. The completely reconstructed catalysts are featured by ultrasmall nanoparticle-interconnected structure with low-crystalline, abundant boundaries/vacancies properties. Benefiting from such a unique structure, the obtained cat.-51.9 possesses high-efficiency OER catalysis and high durability for over hundreds of hours with negligible activity decay at 25.0 and 51.9 °C. Experimental observations and theoretical analyses demonstrate that the boundary–vacancy co-effect can reduce the energy barrier of catalytic reaction and accelerate the OER

kinetics. The coupled array system based on cat.-51.9 and MoO<sub>2</sub>-Ni offers robust water electrolysis operation at 51.9 °C, showing their potential industrial applications in high-temperature water electrolysis. This work uncovers the thermally induced complete reconstruction phenomenon and highlights the potential commercial applications of the completely reconstructed catalysts in high-temperature water electrolysis.

## Supporting Information

Supporting Information is available from the Wiley Online Library or from the author.

## Acknowledgements

This work was supported by the National Natural Science Foundation of China (51521001, 21890751), Foshan Xianhu Laboratory of the Advanced Energy Science and Technology Guangdong Laboratory (XHT2020-003), the China Postdoctoral Science Foundation (2019TQ0306), the National Key Research and Development Program of China (2016YFA0202603). The S/TEM work was performed at the Nanostructure Research Center (NRC), supported by the Fundamental Research Funds for the Central Universities (WUT: 201911012GX, 202011002GX). The authors thank Kwadwo Asare Owusu from Wuhan University of Technology for polishing our manuscript.

## Conflict of Interest

The authors declare no conflict of interest.

## Keywords

alkaline water electrolysis, complete reconstruction, grain/phase boundaries, in situ low-/high-temperature Raman, industrial temperatures, nanowire arrays

Received: February 17, 2020

Revised: August 6, 2020

Published online: September 2, 2020

- [1] A. Buttler, H. Spliethoff, *Renew. Sust. Energ. Rev.* **2018**, *82*, 2440.
- [2] V. R. Stamenkovic, D. Strmcnik, P. P. Lopes, N. M. Markovic, *Nat. Mater.* **2017**, *16*, 57.
- [3] K. Zeng, D. K. Zhang, *Prog. Energy Combust. Sci.* **2010**, *36*, 307.
- [4] X. Y. Lu, J. Pan, E. Lovell, T. H. Tan, Y. H. Ng, R. Amal, *Energy Environ. Sci.* **2018**, *11*, 1898.
- [5] W. R. Cheng, X. Zhao, H. Su, F. M. Tang, W. Che, H. Zhang, Q. H. Liu, *Nat. Energy* **2019**, *4*, 115.
- [6] B. Zhang, X. L. Zheng, O. Voznyy, R. Comin, M. Bajdich, M. García-Melchor, L. L. Han, J. X. Xu, M. Liu, L. R. Zheng, F. P. García de Arquer, C. T. Dinh, F. J. Fan, M. J. Yuan, E. Yassitepe, N. Chen, T. Regier, P. F. Liu, Y. H. Li, P. De Luna, A. Janmohamed, H. L. L. Xin, H. G. Yang, A. Vojvodic, E. H. Sargent, *Science* **2016**, *352*, 333.
- [7] H. M. Sun, Z. H. Yan, F. M. Liu, W. C. Xu, F. Y. Cheng, J. Chen, *Adv. Mater.* **2020**, *32*, 1806326.

- [8] M. Schalenbach, A. R. Zeradjanin, O. Kasian, S. Cherevko, K. J. J. Mayrhofer, *Int. J. Electrochem. Sci.* **2018**, *13*, 1173.
- [9] H. J. Yan, Y. Xie, A. P. Wu, Z. C. Cai, L. Wang, C. G. Tian, X. M. Zhang, H. G. Fu, *Adv. Mater.* **2019**, *31*, 1901174.
- [10] X. Liu, K. Ni, C. J. Niu, R. T. Guo, W. Xi, Z. Y. Wang, J. S. Meng, J. T. Li, Y. W. Zhu, P. J. Wu, Q. Li, J. Luo, X. J. Wu, L. Q. Mai, *ACS Catal.* **2019**, *9*, 2275.
- [11] R. Chen, S.-F. Hung, D. J. Zhou, J. J. Gao, C. J. Yang, H. B. Tao, H. B. Yang, L. P. Zhang, L. L. Zhang, Q. H. Xiong, H. M. Chen, B. Liu, *Adv. Mater.* **2019**, *31*, 1903909.
- [12] M. Chatti, J. L. Gardiner, M. Fournier, B. Johannessen, T. Williams, T. R. Gengenbach, N. Pai, C. Nguyen, D. R. MacFarlane, R. K. Hocking, A. N. Simonov, *Nat. Catal.* **2019**, *2*, 457.
- [13] X. Liu, K. Ni, B. Wen, R. T. Guo, C. J. Niu, J. S. Meng, Q. Li, P. J. Wu, Y. W. Zhu, X. J. Wu, L. Q. Mai, *ACS Energy Lett.* **2019**, *4*, 2585.
- [14] Y. Duan, S. N. Sun, Y. M. Sun, S. B. Xi, X. Chi, Q. H. Zhang, X. Ren, J. X. Wang, S. J. H. Ong, Y. H. Du, L. Gu, A. Grimaud, Z. C. J. Xu, *Adv. Mater.* **2019**, *31*, 1807898.
- [15] E. Fabbri, M. Nachtegaal, T. Binninger, X. Cheng, B.-J. Kim, J. Durst, F. Bozza, T. Graule, R. Schäublin, L. Wiles, M. Pertoso, N. Danilovic, K. E. Ayers, T. Schmidt, *Nat. Mater.* **2017**, *16*, 925.
- [16] Y. Duan, Z.-Y. Yu, S.-J. Hu, X.-S. Zheng, C.-T. Zhang, H.-H. Ding, B.-C. Hu, Q.-Q. Fu, Z.-L. Yu, X. Zheng, J.-F. Zhu, M.-R. Gao, S.-H. Yu, *Angew. Chem., Int. Ed.* **2019**, *58*, 15772.
- [17] S. Jin, *ACS Energy Lett.* **2017**, *2*, 1937.
- [18] L.-A. Stern, L. G. Feng, F. Song, X. L. Hu, *Energy Environ. Sci.* **2015**, *8*, 2347.
- [19] T. Z. Wu, S. N. Sun, J. J. Song, S. B. Xi, Y. H. Du, B. Chen, W. A. Sasangka, H. B. Liao, C. L. Gan, G. G. Scherer, L. Zeng, H. J. Wang, H. Li, A. Grimaud, Z. C. J. Xu, *Nat. Catal.* **2019**, *2*, 763.
- [20] S. Niu, W.-J. Jiang, Z. X. Wei, T. Tang, J. M. Ma, J.-S. Hu, L.-J. Wan, *J. Am. Chem. Soc.* **2019**, *141*, 7005.
- [21] B. W. Zhang, K. Jiang, H. T. Wang, S. Hu, *Nano Lett.* **2019**, *19*, 530.
- [22] Y. P. Zhu, H.-C. Chen, C.-S. Hsu, T.-S. Lin, C.-J. Chang, S. C. Chang, L.-D. Tsai, H. M. Chen, *ACS Energy Lett.* **2019**, *4*, 987.
- [23] S.-F. Hung, Y. P. Zhu, G.-Q. Tzeng, H.-C. Chen, C.-S. Hsu, Y.-F. Liao, H. Ishii, N. Hiraoka, H. M. Chen, *ACS Energy Lett.* **2019**, *4*, 2813.
- [24] S. J. Peng, F. Gong, L. L. Li, D. S. Yu, D. X. Ji, T. R. Zhang, Z. Hu, Z. Q. Zhang, S. L. Chou, Y. H. Du, S. Ramakrishna, *J. Am. Chem. Soc.* **2018**, *140*, 13644.
- [25] T. Zhang, M.-Y. Wu, D.-Y. Yan, J. Mao, H. Liu, W.-B. Hu, X.-W. Du, T. Ling, S.-Z. Qiao, *Nano Energy* **2018**, *43*, 103.
- [26] D. Friebel, M. W. Louie, M. Bajdich, K. E. Sanwald, Y. Cai, A. M. Wise, M.-J. Cheng, D. Sokaras, T.-C. Weng, R. Alonso-Mori, R. C. Davis, J. R. Bargar, J. K. Nørskov, A. Nilsson, A. T. Bell, *J. Am. Chem. Soc.* **2015**, *137*, 1305.
- [27] C. L. Xie, Z. Q. Niu, D. Kim, M. F. Li, P. D. Yang, *Chem. Rev.* **2020**, *120*, 1184.
- [28] R. G. Mariano, K. McKelvey, H. S. White, M. W. Kanan, *Science* **2017**, *358*, 1187.
- [29] J. Q. Zhu, Z.-C. Wang, H. J. Dai, Q. Q. Wang, R. Yang, H. Yu, M. Z. Liao, J. Zhang, W. Chen, Z. Wei, N. Li, L. J. Du, D. X. Shi, W. L. Wang, L. X. Zhang, Y. Jiang, G. Y. Zhang, *Nat. Commun.* **2019**, *10*, 1348.
- [30] Y. J. Pang, J. Li, Z. Y. Wang, C.-S. Tan, P.-L. Hsieh, T.-T. Zhuang, Z.-Q. Liang, C. Q. Zou, X. Wang, P. De Luna, J. P. Edwards, Y. Xu, F. W. Li, C.-T. Dinh, M. Zhong, Y. H. Lou, D. Wu, L.-J. Chen, E. H. Sargent, D. Sinton, *Nat. Catal.* **2019**, *2*, 251.
- [31] Z. H. Li, M. F. Shao, H. L. An, Z. X. Wang, S. M. Xu, M. Wei, D. G. Evans, X. Duan, *Chem. Sci.* **2015**, *6*, 6624.
- [32] Y. P. Liu, X. Liang, L. Gu, Y. Zhang, G.-D. Li, X. X. Zou, J.-S. Chen, *Nat. Commun.* **2018**, *9*, 2609.
- [33] G. Chen, Y. P. Zhu, H. M. Chen, Z. W. Hu, S.-F. Hung, N. N. Ma, J. Dai, H.-J. Lin, C.-T. Chen, W. Zhou, Z. P. Shao, *Adv. Mater.* **2019**, *31*, 1900883.